

Benchmarking maximum-likelihood state estimation with an entangled two-cavity state

V. Métillon,¹ S. Gerlich,^{1,*} M. Brune,¹ J.M. Raimond,¹ P. Rouchon,^{2,3} and I. Dotsenko¹

¹*Laboratoire Kastler Brossel, Collège de France, CNRS, ENS-Université PSL, Sorbonne Université, 11 place Marcelin Berthelot, F-75231 Paris, France*

²*Centre Automatique et Systèmes, Mines-ParisTech,*

PSL Research University, 60 Boulevard Saint-Michel, 75006 Paris, France

³*INRIA Paris, 2 rue Simone Iff, 75012 Paris, France*

(Dated: August 9, 2021)

The efficient quantum state reconstruction algorithm described in [P. Six *et al.*, Phys. Rev. A **93**, 012109 (2016)] is experimentally implemented on the non-local state of two microwave cavities entangled by a circular Rydberg atom. We use information provided by long sequences of measurements performed by resonant and dispersive probe atoms over time scales involving the system decoherence. Moreover, we benefit from the consolidation, in the same reconstruction, of different measurement protocols providing complementary information. Finally, we obtain realistic error bars for the matrix elements of the reconstructed density operator. These results demonstrate the pertinence and precision of the method, directly applicable to any complex quantum system.

Quantum state reconstruction or tomography is an essential operation in quantum science. It has a key role in parameter estimation, quantum metrology and studies of decoherence. It is instrumental for quantum process tomography, central in the benchmarking of quantum technologies. Many reconstruction methods have been proposed [1–8] and implemented [9–18].

The maximum likelihood (ML) estimation is widely used. It requires a large number of realizations of the state (density operator ρ). Generally, one performs a single instantaneous measurement described by a positive operator-valued measure on each of them. An iterative algorithm determines the ML estimate, ρ_{ML} , of ρ maximizing the likelihood of observed experimental results [1, 19]. In principle, more information could be obtained through a composite sequence of measurements (intertwined with system evolution and decoherence), with a possibly different set of measurements for each realization. At each step of the standard ML iteration, and for each realization one then must compute the time evolution through the measurement sequence to get the updated likelihood, making this procedure numerically heavy.

A recently proposed ML implementation method [20], inspired by the ‘past quantum state’ formalism [21], overcomes efficiently this difficulty. The complete sequence for each realization, including information on experimental imperfections, is encapsulated in an ‘effect matrix’, computed only once for all ML iterations. Moreover, a unique feature of this method is that it provides a direct estimate of the precision of the reconstructed density operator matrix elements. This result leads to a simple practical approach to the important problem of estimating the reconstruction precision [22–25].

In this Letter, we experimentally benchmark the power, pertinence and precision of this new method applied to the non-local state of two fields stored in two su-

perconducting microwave cavities. The entangled state is prepared and probed by individual circular Rydberg atoms interacting sequentially with these two fields. We efficiently reconstruct the two-cavity state in a large Hilbert space by combining the results of different types of atom-cavity interactions, by taking into account imperfections and decoherence and by using all information from long sequences of probe atoms.

Before turning to the experiment, let us recall briefly the main results of [20]. The probability $p_r(\rho)$ for observing the measurement outcomes of realization r in the unknown state ρ reads

$$p_r(\rho) = \text{Tr} \left[\mathbb{K}_{N_r}^{(r)} \circ \mathbb{K}_{N_r-1}^{(r)} \circ \dots \circ \mathbb{K}_2^{(r)} \circ \mathbb{K}_1^{(r)}(\rho) \right], \quad (1)$$

where $\{\mathbb{K}_j^{(r)}\}$ is a sequence of N_r time-ordered quantum maps taking into account all effects in the specific measurement sequence: measurement backaction, unitary evolutions, relaxation, etc. Knowing ρ , the probability of all measurement records in R independent realizations is the likelihood function $\mathcal{P}(\rho) = \prod_{r=1}^R p_r(\rho)$, which is maximized by ρ_{ML} .

The key ingredient in [20] is to write $p_r(\rho) = c_r \text{Tr}[\rho E^{(r)}]$, where the effect matrix $E^{(r)}$ reads

$$E^{(r)} = \tilde{\mathbb{K}}_1^{(r)} \circ \tilde{\mathbb{K}}_2^{(r)} \circ \dots \circ \tilde{\mathbb{K}}_{N_r-1}^{(r)} \circ \tilde{\mathbb{K}}_{N_r}^{(r)}(I/\mathcal{N}_{\text{H}}). \quad (2)$$

The constant c_r is a function of the measurement outcomes in realization r . It does not depend on ρ and is thus irrelevant for the ML optimization. The ‘adjoint’ maps, $\{\tilde{\mathbb{K}}_j^{(r)}\}$ [26], are applied in time-reversed order to a normalized identity operator I (\mathcal{N}_{H} is a Hilbert space dimension). The effect matrix is, in the past quantum state picture [21], the best estimate of the initial density matrix in realization r [30]. Since the $E^{(r)}$ s do not depend on ρ , they can be computed once before ML optimization, making the latter efficient even for complex

sequences. Notably, the method can efficiently consolidate the results of different arbitrary measurement types and sequences. All measurements contribute to the reconstruction, even if they are performed only in a small number of realizations.

The method [20] also provides the confidence interval $\sigma(\langle A \rangle)$ for any observable mean value $\langle A \rangle = \text{Tr}[A\rho_{\text{ML}}]$ [26]. With $A = (|p\rangle\langle q| + |q\rangle\langle p|)/2$ or $A = i(|p\rangle\langle q| - |q\rangle\langle p|)/2$ ($\{|p\rangle\}$ is a Hilbert space basis), we get directly the error bars of the real and imaginary parts of $(\rho_{\text{ML}})_{pq}$. This direct estimation of the reconstruction quality, much simpler than other proposals [22–25], makes this method particularly appealing.

The experimental set-up is depicted in Fig. 1(a). The two cavities, C_1 and C_2 , have resonance frequencies $\omega_{c,1}/2\pi \approx \omega_{c,2}/2\pi \approx 51$ GHz. Their lifetimes are $T_{c,1} = 10$ ms and $T_{c,2} = 25$ ms at a 1.5 K temperature, with an average thermal photon number $n_{\text{th}} = 0.25$. At 0.8 K, we have $T_{c,1} = 20$ ms, $T_{c,2} = 50$ ms and $n_{\text{th}} = 0.06$. Sources S_1 and S_2 can inject coherent fields with controllable complex amplitudes in C_1 and C_2 . The cavity states are manipulated by a sequence of individual circular rubidium Rydberg atoms (atomic states $|g\rangle$ and $|e\rangle$ with principal quantum numbers 50 and 51, atomic resonance frequency $\omega_a/2\pi = 51$ GHz, atomic lifetime $T_a \approx 30$ ms) [31, 32]. Samples with 0.1 to 0.2 atoms on the average are prepared in $|g\rangle$ in the excitation zone B out of a velocity-selected thermal atomic beam (flight time between the cavities 0.36 ms). The common vacuum Rabi frequency measuring the atom-cavity coupling is $\Omega_0/2\pi = 49$ kHz. Applying an electric field across the mirrors of C_i with voltages sources V_i , we can tune ω_a relative to $\omega_{c,i}$ through the Stark effect, quadratically shifting atomic circular levels, and thus switch between resonant ($\delta_{ac} = \omega_a - \omega_c = 0$) and dispersive ($|\delta_{ac}| > \Omega_0$) interactions and control the atom-cavity interaction time. The Ramsey zones R_1 and R_2 , fed by source S_R , are used to manipulate the atomic state with classical microwave pulses resonant on the $|g\rangle \rightarrow |e\rangle$ transition. The atoms are finally measured in the detector D by state-selective field-ionisation (detection efficiency ≈ 0.5).

We apply the reconstruction to the non-local entangled state $|\Psi\rangle = (|1, 0\rangle + |0, 1\rangle)/\sqrt{2}$, where one photon is coherently shared by C_1 and C_2 . Its preparation is reminiscent of that of an entangled state of two modes of the same cavity [33]. An ‘entangling’ atom, A_1 , is prepared in $|e\rangle$ in R_1 and tuned to resonance with the initially empty cavities. It experiences a $\pi/2$ -Rabi rotation in C_1 and a state-swap with C_2 (π -Rabi rotation). Due to the $\delta = \omega_{c,2} - \omega_{c,1} = 2\pi \times 8.9$ kHz detuning between C_1 and C_2 , the state evolves as $|\Psi(t)\rangle = (|1, 0\rangle + e^{i\delta t}|0, 1\rangle)/\sqrt{2}$ within a proper phase reference and with the time origin $t = 0$ set at the end of the π -Rabi pulse in C_2 . Because of the probabilistic Poisson distribution of atoms in a sample and their non-ideal detection, the state $|\Psi\rangle$ is considered to be prepared if we detect only one atom in

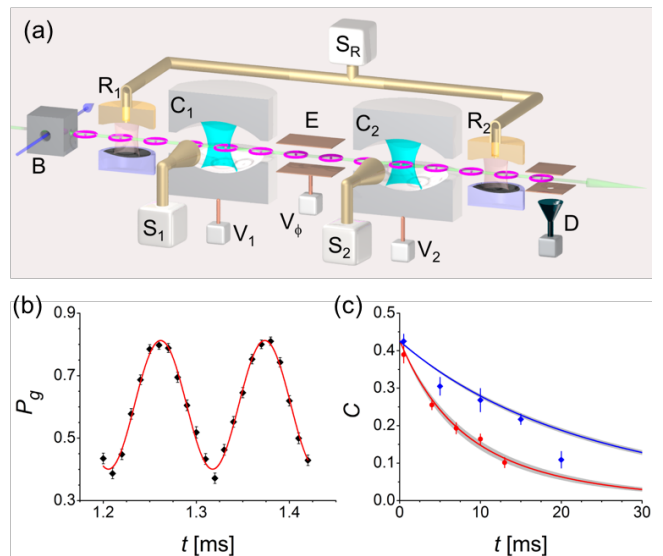


FIG. 1. Preparation and detection of a two-cavity entangled state. (a) Scheme of the experimental setup with two microwave cavities (C_1 , C_2) and circular Rydberg atoms, see text for details. (b) Quantum beat note between the two components of the non-local state $|\Psi(t)\rangle$ directly measured as $P_g(t)$. Error bars are statistical, the solid line is a fit with $f(x) = y_0 - C/2 \cos(\delta x + \varphi)$ ($0 \leq C \leq 1$), leading to a $C_0 = 0.4$ contrast. (c) Time decay of C revealing the decoherence of the two-cavity state. The experimental points are obtained by fitting the $P_g(t)$ oscillation signals around different t s for two cavity temperatures: 0.8 K (blue) and 1.5 K (red). The solid lines result from numerical predictions with C_0 as the only adjustable parameter. The shaded areas are numerical uncertainties resulting from the finite accuracy (± 1 ms) on the measured cavity lifetimes. The residual variance between the curves and the ensemble of points is compatible with the error bars, except for the longest time $t = 20$ ms. The measured frequency drift of the two-cavity setup of several tens of Hz per hour (approximate acquisition time for the measurement with $t = 20$ ms) results in a phase diffusion significantly reducing the oscillation contrast at this timescale.

$|g\rangle$. The probability to have another non-detected atom during the entanglement preparation is about 3%.

For an elementary check of the state preparation, we use a probe atom, A_2 , undoing the action of A_1 [33]. Initially in $|g\rangle$, A_2 performs a π -Rabi rotation in C_1 and a $\pi/2$ -Rabi rotation in C_2 . The probability P_g for detecting A_2 in $|g\rangle$ at a delay time t after A_1 is ideally $P_g = [1 - \cos(\delta t + \varphi)]/2$ (φ is a constant phase determined by the timing details). The oscillations of P_g for short times t around 1.3 ms are presented in Fig. 1(b). They have a finite contrast $C = C_0 = 0.4$, due to experimental imperfections. For larger times, C decays with t , as shown in Fig. 1(c), due to photon loss at a rate depending on the cavities temperature, 1.5 K (0.8 K) for the red (blue) dots. The solid curves are numerical predictions with C_0 as the only adjustable parameter.

We now proceed to a ML reconstruction of the two-

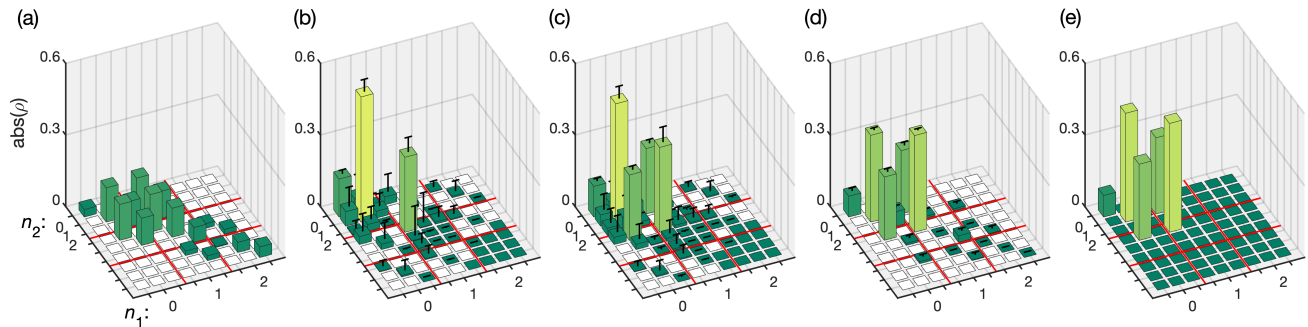


FIG. 2. Absolute values of density matrix elements in a 3×3 two-cavity Hilbert space. Red guiding lines enclose areas with the same photon number in C_1 ; n_1 and n_2 are photon numbers in C_1 and C_2 , respectively. (a) Reconstruction with single resonant atom measurements. (b) Reconstruction with QND parity measurement. (c) Reconstruction with both resonant and dispersive data of (a) and (b). (d) Reconstruction with sequences of several resonant measurements. Error bars $\sigma(\text{abs}(\rho_{\text{ML}}))$ in (a) are of the order of 0.5 and are not shown. Error bars smaller than 10^{-3} are not shown in plots (b)-(d). (e) Numerical prediction $\text{abs}(\rho_{\text{TH}})$ of the prepared state. The exact values of all reconstructed density matrices in the full 5×5 Hilbert space, together with their real and complex error bars, are given in [26].

cavity state. We measure it by choosing between two types of the atom-cavity interaction: dispersive and resonant. We set resonant atoms, prepared in $|g\rangle$, to undergo the same temporal sequence as A_2 . In addition to the unitary evolutions and relaxation in C_1 and C_2 , the quantum map includes the detection imperfections as well as the small probability that a second, spurious atom present in the probe sample has escaped detection [26]. Dispersive atoms are set to implement a quantum non-demolition (QND) measurement of the joint photon-number parity of the two cavities by setting $\delta_{ac}/2\pi \approx 60$ kHz [31]. An atomic coherence, prepared by a $\pi/2$ pulse in R_1 , is shifted by π for each photon present in either cavity. This shift is probed by a $\pi/2$ pulse in R_2 , the phase of which is set to maximize the probability for detecting the atom in $|g\rangle$ when both cavities are in the vacuum state. These dispersive probes do not change the photon numbers in C_1 and C_2 . The measurements are intertwined with maps representing the free rotation of the two-cavity state at the frequency difference δ and the cavities relaxation. Optional field displacements are performed by S_1 and S_2 before the measurement. All quantum maps, including measurement imperfections, are given in [26].

We first analyse all data obtained with a single resonant probe that led to the results of Fig. 1(b) at 0.8 K. The sequence involves a free evolution and relaxation during time t followed by a single resonant probe. The reconstruction is based on 3913 realizations and performed in a tensor Hilbert space of dimension 5×5 (photon numbers n from 0 to 4 in each cavity). The ML estimate, ρ_{ML} , is presented in Fig. 2(a). For the sake of visibility, we plot only the absolute values of the ρ_{ML} elements for n from 0 to 2 (the full ρ_{ML} is shown in [26]).

Note that all two-cavity states of the form $|\Xi\rangle = (|n_1, n_2\rangle + |n_1-1, n_2+1\rangle)/\sqrt{2}$ lead, for a resonant probe, to oscillations of $P_g(t)$ with the same frequency as those

produced by $|\Psi(t)\rangle$, since their components also differ by only one photon and thus their energy difference is also $\hbar\delta$. The reconstructed ρ_{ML} is thus a mixture of entangled states $|\Xi\rangle$. They appear with different weights, since the dependence of the Rabi oscillation frequency on the photon number brings ambiguous information on it. Due to this photon-number indetermination, the reconstruction error bars [not shown in Fig. 2(a)] are extremely large, of the order of 0.5 for all elements.

It is also important to note that the ML reconstruction may be blind to some elements of ρ . Writing $p_r(\rho) = \sum_{p,q} (\rho_{pq})^* E_{pq}^{(r)}$ in a generic basis $\{|p\rangle\}$, we see that $p_r(\rho)$ does not depend on ρ_{pq} if $E_{pq}^{(r)} = 0$ for specific p and q values. More generally, if no measurement contains information on ρ_{pq} and thus $\sum_r |E_{pq}^{(r)}| = 0$, the likelihood is independent of ρ_{pq} and we get no more information on this specific matrix element than that provided by the positivity and unit trace of ρ . The blank elements in Fig. 2(a) correspond to those, on which the set of effect matrices provides no information.

An alternative measurement strategy providing better photon-number discrimination is based on QND joint parity measurements following adjustable coherent field injections (amplitudes α_1 and α_2) in the cavities [34]. This procedure amounts to a direct determination of the two-cavity Wigner function, $(\pi^2/4)W(\alpha_1, \alpha_2)$, at one point in the four-dimensional phase-space [15]. Here, for simplicity, we choose to inject in only one cavity at a time with 20 values of the injection amplitude ranging from 0 to 2.

Figure 2(b) shows the reconstructed state using 12200 realizations, each with 40 dispersive atom samples sent over a 4-ms time period. We now fully benefit from the efficiency of the method [20] for a long sequence of successive measurements in a single realization. The reconstruction is sensitive to the photon number (diagonal

elements) and to local, single-mode coherences between states $|n\rangle$ and $|n'\rangle$ of the same cavity. Hence, the reconstructed state mainly includes $|1, 0\rangle\langle 1, 0|$ and $|0, 1\rangle\langle 0, 1|$. The significant contribution of $|0, 0\rangle\langle 0, 0|$ is due to atom and cavity relaxation during the state preparation. All other elements of ρ_{ML} on which we get information are zero within their error bars. Note that this measurement does not provide any information on non-local coherences between the two cavities (blank elements in the figure).

The resonant and dispersive measurements provide complementary information on ρ_{ML} : the former is sensitive to non-local coherences, while the latter accurately reconstructs the photon-number probabilities. The reconstructed state consolidating the resonant and QND measurements data described above is shown in Fig. 2(c). Now, the dominant elements are the populations and coherences expected for $|\Psi\rangle$, showing that the data consolidation significantly improves the reconstruction.

As a reference to this reconstruction, Fig. 2(e) presents a numerical prediction, ρ_{TH} , of the prepared state. The model includes cavity and atomic relaxations, leading to the vacuum state population of 0.09. It also includes a reduction of the coherences by 30% estimating the effect of stray electric fields inhomogeneity inside the atomic sample over the flight between C_1 and C_2 . These stray fields perturb the phase of A_1 and, thus, the phase between the $|1, 0\rangle$ and $|0, 1\rangle$ components of ρ_{TH} . They contribute to the contrast reduction observed in Fig. 1(b).

The method does not require that the successive measurements commute, characteristic of the QND probes. We illustrate this unique feature by reconstructing the state with a long sequence of resonant probe samples. Each of them considerably changes the following measurement outcomes through its possible photon emission or absorption. We can nevertheless get useful information out of long sequences of non-ideally detected samples with a precise knowledge of the associated maps. The corresponding experiment involves 40 resonant atomic samples separated by 0.2 ms with, on average 0.15 atoms per sample. The reconstruction result based on 18000 realizations is presented in Fig. 2(d). The possibility of detecting more than one atom per realization indeed considerably improves the photon number determination with respect to Fig. 2(a). In addition, the long measurement duration improves the discrimination of small and large n 's, which have different lifetimes. Finally, using many samples significantly increases the information acquisition rate per realization.

We compute the fidelity $F(\rho, \sigma) = [\text{Tr}\sqrt{\sqrt{\rho}\sigma\sqrt{\rho}}]^2$ between two different states ρ and σ in order to compare them. The fidelity of the reconstructed states of Fig. 2(a)-(d) with respect to the theoretical one [Fig. 2(e)] is 0.29, 0.85, 0.96 and 0.78, respectively. It is similar for the states (b) and (d), because the former is better in reproducing the expected populations in $|1, 0\rangle$ and $|0, 1\rangle$, while the former is better in the estimation

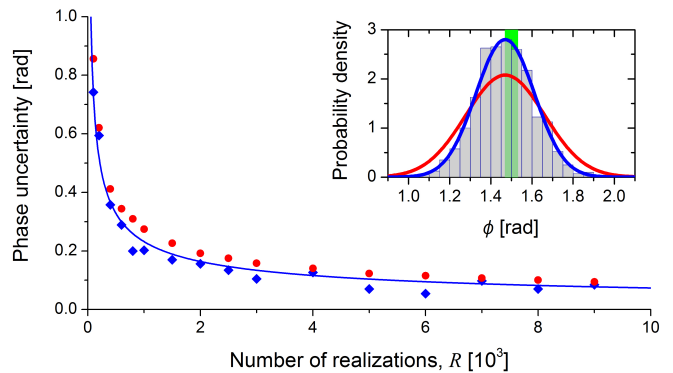


FIG. 3. Statistical properties of the phase uncertainty. Blue diamonds: dispersion $\tilde{\sigma}_{\phi,R}$ of the reconstructed ϕ values versus the number of realizations R . Solid line: fit with a statistical dispersion function. Red circles: mean value of computed $\sigma(\phi)$. Note that having the limited set of all experimental realizations, we have fewer independent statistical sets of large size R . Therefore, there are fewer independent reconstructions and hence the larger statistical variance of reconstruction results for large R . Inset: distribution of ϕ from 800 reconstructions on samples with $R = 2000$ realizations (histogram). Blue (red) line: Gaussian with width $\tilde{\sigma}_{\phi,R}$ ($\langle\sigma(\phi)\rangle_R$). Green band: independently measured confidence interval for ϕ_a .

of coherences. The large fidelity value for the state in (c) highlights the interest of consolidating many different measurements in the reconstruction, a key feature of our approach.

The method provides error bars for the density operator elements. In order to check that they faithfully describe the reconstruction precision, we apply the method to the estimation of a simple parameter and compare its predicted uncertainty to its experimental dispersion observed in many reconstructions. We have chosen to estimate the phase ϕ_a of the initial state $|\Psi_\phi\rangle = (|1, 0\rangle + e^{i\phi_a}|0, 1\rangle)/\sqrt{2}$, which is an essential characteristic of the prepared entangled state. This phase is tuned by applying an electric field across the electrodes E , sandwiched between C_1 and C_2 [Fig. 1(a)]. This field changes the phase of the coherence of A_1 , which is finally imprinted into the phase of the two-cavity state. In the following, we prepare $|\Psi_\phi\rangle$ with $\phi_a = 1.50 \pm 0.03$ rad, independently calibrated with Ramsey spectroscopy.

We implement a bootstrapping approach to estimate the reconstruction precision as a function of the sample size R (number of realizations used for one reconstruction), see [26] for more details. We calculate the standard deviation $\tilde{\sigma}_{\phi,R}$ of the reconstructed values of ϕ and the mean value $\langle\sigma(\phi)\rangle_R$ of the computed error bar $\sigma(\phi)$. Figure 3 shows $\tilde{\sigma}_{\phi,R}$ (blue diamonds) and $\langle\sigma(\phi)\rangle_R$ (red circles) versus R . Their values are nearly equal, exhibiting the accuracy of the error bar prediction. The solid line is a fit of $\tilde{\sigma}_{\phi,R}$ to a function $y(x) = A/\sqrt{x}$ confirming that the measured deviations have a purely statistical origin.

The slight systematic excess of $\langle\sigma(\phi)\rangle_R$ with respect to $\tilde{\sigma}_{\phi,R}$ is potentially due to higher order correcting terms in the asymptotic expansion versus R of Bayesian variances underlying $\langle\sigma(\phi)\rangle_R$ that corresponds only to the dominant term of order $1/\sqrt{R}$ [29]. The inset in Fig. 3 shows the histogram of the individual ϕ values for $R = 2000$. The green band gives the calibration of ϕ_a and its uncertainty. The blue (red) line is a Gaussian with width $\tilde{\sigma}_{\phi,R}$ ($\langle\sigma(\phi)\rangle_R$). These results confirm that the method provides realistic error bars on ρ_{ML} .

In summary, we have experimentally demonstrated on a two-cavity entangled state the pertinence and precision of the ML state reconstruction method proposed in [20]. We have shown that it efficiently takes into account data provided by different measurement strategies as well as the system evolution during the measurement sequence. It integrates easily the description of measurement imperfections. We have shown that it provides realistic error bars for the reconstructed density matrix elements. The method is quite general and can be applied to nearly any quantum system and any measurement protocol, well beyond demonstrations in cavity or circuit QED [20]. If the initial quantum state is known, the method can also be efficiently implemented for the parameter estimation [36]. Finally, the analysis of the structure of the effect matrices provides a guide for designing adaptive reconstruction procedures [37–39] by selecting optimal measurements.

We acknowledge support by European Research Council (DECLIC and TRENSCRYBE projects), by European Community (SIQS project) and by the Agence Nationale de la Recherche (QuDICE project).

* Current affiliation: Faculty of Physics, University of Vienna, Boltzmannngasse 5, A-1090 Vienna, Austria

- [1] M. Paris and J. Řeháček, *Quantum State Estimation*, Springer, Berlin, Heidelberg (2004)
- [2] Y. S. Teo, *Introduction to Quantum-State Estimation*, World Scientific, (2015)
- [3] A. Silberfarb, P. S. Jessen, and I. H. Deutsch, *Quantum State Reconstruction via Continuous Measurement*, Phys. Rev. Lett. **95**, 030402 (2005).
- [4] D. Gross, Y. K. Liu, S. T. Flammia, S. Becker, and J. Eisert, *Quantum State Tomography via Compressed Sensing*, Phys. Rev. Lett. **105**, 150401 (2010).
- [5] Y. S. Teo, H. Zhu, B.-G. Englert, J. Řeháček, and Z. Hradil, *Quantum-State Reconstruction by Maximizing Likelihood and Entropy*, Phys. Rev. Lett. **107**, 020404 (2011).
- [6] B. Qi, Z. Hou, L. Li, D. Dong, G. Xiang, and G. Guo, *Quantum state tomography via linear regression estimation*, Sci. Rep. **3**, 3496 (2013).
- [7] A. Kyrillidis, A. Kalev, D. Park, S. Bhojanapalli, C. Caramanis, and S. Sanghavi, *Provable compressed sensing quantum state tomography via non-convex methods*, npj Quantum Information **4**, 36 (2018).
- [8] G. Torlai, G. Mazzola, J. Carrasquilla, M. Troyer, R. Melko, and G. Carleo, *Neural-network quantum state tomography*, Nature Physics **14**, 447450 (2018).
- [9] A. I. Lvovsky, H. Hansen, T. Aichele, O. Benson, J. Mlynek, and S. Schiller, *Quantum State Reconstruction of the Single-Photon Fock State*, Phys. Rev. Lett. **87**, 050402 (2001).
- [10] H. Hffner, W. Hnsel, C. F. Roos, J. Benhelm, D. Chekalkar, M. Chwalla, T. Krber, U. D. Rapol, M. Riebe, P. O. Schmidt, C. Becher, O. Ghne, W. Dr, and R. Blatt, *Scalable multiparticle entanglement of trapped ions*, Nature **438**, 643646 (2005).
- [11] G. Zambra, A. Andreoni, M. Bondani, M. Gramegna, M. Genovese, G. Brida, A. Rossi, and M. G. A. Paris, *Experimental Reconstruction of Photon Statistics without Photon Counting*, Phys. Rev. Lett. **95**, 063602 (2005).
- [12] W.-B. Gao, C.-Y. Lu, X.-C. Yao, P. Xu, O. Ghne, A. Goebel, Y.-A. Chen, C.-Z. Peng, Z.-B. Chen, and J.-W. Pan, *Experimental demonstration of a hyper-entangled ten-qubit Schrödinger cat state*, Nature Physics **6**, 331-335 (2010).
- [13] D. Giovannini, J. Romero, J. Leach, A. Dudley, A. Forbes, and M. J. Padgett, *Characterization of High-Dimensional Entangled Systems via Mutually Unbiased Measurements*, Phys. Rev. Lett. **110**, 143601 (2013).
- [14] N. Bent, H. Qassim, A. A. Tahir, D. Sych, G. Leuchs, L. L. Sánchez-Soto, E. Karimi, and R. W. Boyd, *Experimental Realization of Quantum Tomography of Photonic Qudits via Symmetric Informationally Complete Positive Operator-Valued Measures*, Phys. Rev. X **5**, 041006 (2015).
- [15] C. Wang, Y. Y. Gao, P. Reinhold, R. W. Heeres, N. Ofek, K. Chou, C. Axline, M. Reagor, J. Blumoff, K. M. Sliwa, L. Frunzio, S. M. Girvin, L. Jiang, M. Mirrahimi, M. H. Devoret, and R. J. Schoelkopf, *A Schrödinger cat living in two boxes*, Science **352**, 1087 (2016).
- [16] C. A. Riofro, D. Gross, S. T. Flammia, T. Monz, D. Nigg, R. Blatt, J. Eisert, *Experimental quantum compressed sensing for a seven-qubit system*, Nature Communications **8**, 15305 (2017).
- [17] A. Steffens, C. A. Riofro, W. McCutcheon, I. Roth, B. A. Bell, A. McMillan, M. S. Tame, J. G. Rarity, and J. Eisert, *Experimentally exploring compressed sensing quantum tomography*, Quantum Sci. Technol. **2**, 025005 (2017).
- [18] D. Ahn, Y.S. Teo, H. Jeong, F. Bouchard, F. Hufnagel, E. Karimi, D. Koutný, J. Řeháček, Z. Hradil, G. Leuchs, and L. L. Sánchez-Soto, *Adaptive Compressive Tomography with No a priori Information*, Phys. Rev. Lett. **122**, 100404 (2019).
- [19] Z. Hradil, *Quantum-state estimation*, Phys. Rev. A **55**, 1561 R (1997).
- [20] P. Six, Ph. Campagne-Ibarcq, I. Dotsenko, A. Sarlette, B. Huard, and P. Rouchon, *Quantum state tomography with noninstantaneous measurements, imperfections, and decoherence*, Phys. Rev. A **93**, 012109 (2016).
- [21] S. Gammelmark, B. Julsgaard, and K. Mølmer, *Past quantum states of a monitored system*, Phys. Rev. Lett. **111**, 160401 (2013).
- [22] M. Christandl and R. Renner, *Reliable Quantum State Tomography*, Phys. Rev. Lett. **109**, 120403 (2012).
- [23] S. T. Flammia, D. Gross, Y. K. Liu, and J. Eisert, *Quantum tomography via compressed sensing: Error bounds,*

- sample complexity, and efficient estimators*, New J. Phys. **14**, 095022 (2012).
- [24] R. Blume-Kohout, *Robust error bars for quantum tomography*, arXiv:1202.5270.
- [25] P. Faist and R. Renner, *Practical and Reliable Error Bars in Quantum Tomography*, Phys. Rev. Lett. **117**, 010404 (2016).
- [26] See Supplemental Material at [...] for additional experimental and theoretical details, which includes Refs. [27–29].
- [27] S. Haroche and J.M. Raimond, *Exploring the Quantum: atoms, cavities and photons*, Oxford University Press, Oxford (2006).
- [28] Xingxing Zhou, *Field locked to Fock state by quantum feedback with single photon corrections*, PhD thesis, Université Pierre et Marie Curie - Paris VI (2012), <https://tel.archives-ouvertes.fr/tel-00737657>.
- [29] P. Six and P. Rouchon, *Feedback Stabilization of Controlled Dynamical Systems*, chapter *Asymptotic expansions of Laplace integrals for quantum state tomography*, Lecture Notes in Control and Information Sciences 473, pp. 307–327, Springer (2017).
- [30] T. Rybarczyk, B. Peaudecerf, M. Penasa, S. Gerlich, B. Julsgaard, K. Mølmer, S. Gleyzes, M. Brune, J.-M. Raimond, S. Haroche, and I. Dotsenko, *Forward-backward analysis of the photon-number evolution in a cavity*, Phys. Rev. A **91**, 062116 (2015).
- [31] S. Gleyzes, S. Kuhr, C. Guerlin, J. Bernu, S. Deléglise, U. Busk Hoff, M. Brune, J.-M. Raimond, and S. Haroche, *Quantum jumps of light recording the birth and death of a photon in a cavity*, Nature (London) **446**, 297 (2007).
- [32] C. Guerlin, J. Bernu, S. Delglise, C. Sayrin, S. Gleyzes, S. Kuhr, M. Brune, J.-M. Raimond, and S. Haroche, *Progressive field-state collapse and quantum non-demolition photon counting*, Nature (London) **448**, 889 (2007).
- [33] A. Rauschenbeutel, P. Bertet, S. Osnaghi, G. Nogues, M. Brune, J. M. Raimond, and S. Haroche, *Controlled entanglement of two field modes in a cavity quantum electrodynamics experiment*, Phys. Rev. A **64**, 050301(R) (2001).
- [34] S. Deléglise, I. Dotsenko, C. Sayrin, J. Bernu, M. Brune, J.M. Raimond, and S. Haroche, *Reconstruction of non-classical cavity field states with snapshots of their decoherence*, Nature (London) **455**, 510 (2008).
- [35] B. Peaudecerf, C. Sayrin, X. Zhou, T. Rybarczyk, S. Gleyzes, I. Dotsenko, J. M. Raimond, M. Brune, and S. Haroche, *Quantum feedback experiments stabilizing Fock states of light in a cavity*, Phys. Rev. A **87**, 042320 (2013).
- [36] Pierre Six, *Estimation d'état et de paramètres pour les systèmes quantiques ouverts*, PhD thesis, PSL Research University (2016), <https://tel.archives-ouvertes.fr/tel-01511698v1>.
- [37] B. Qi, Z. Hou, Y. Wang, D. Dong, H.-S. Zhong, L. Li, G.-Y. Xiang, H. M. Wiseman, C.-F. Li, and G.-C. Guo, *Adaptive quantum state tomography via linear regression estimation: Theory and two-qubit experiment*, npj Quantum Information **3**, 19 (2017).
- [38] L. Pereira, L. Zambrano, J. Cortés-Vega, S. Niklitschek, and A. Delgado, *Adaptive quantum tomography in high dimensions*, Phys. Rev. A **98**, 012339 (2018).
- [39] G. I. Struchalin, E. V. Kovalkov, S. S. Straupe, and S. P. Kulik, *Adaptive quantum tomography of high-dimensional bipartite systems*, Phys. Rev. A **98**, 032330 (2018).

Supplementary Information: Benchmarking maximum-likelihood state estimation with an entangled two-cavity state

V. Métilion,¹ S. Gerlich,^{1,*} M. Brune,¹ J.M. Raimond,¹ P. Rouchon,^{2,3} and I. Dotsenko¹

¹*Laboratoire Kastler Brossel, Collège de France, CNRS, ENS-Université PSL,
Sorbonne Université, 11 place Marcelin Berthelot, F-75231 Paris, France*

²*Centre Automatique et Systèmes, Mines-ParisTech,
PSL Research University, 60 Boulevard Saint-Michel, 75006 Paris, France*

³*INRIA Paris, 2 rue Simone Iff, 75012 Paris, France*

(Dated: August 9, 2021)

We present in Section I all quantum maps describing the evolution of the two-cavity state in our experiment and the explicit form of all the effect matrices corresponding to the three experimental sequences described in the main paper. In Section II, we summarize the optimization algorithm used to find the density matrix ρ_{ML} maximizing the likelihood of the measured results. Section III presents the evaluation of the reconstruction precision and, in particular, that of the error bars of the matrix elements of ρ_{ML} . Finally, in Section IV, we show all reconstructed density matrices in the full Hilbert space with a dimension 5×5 , used in the maximum likelihood optimization.

I. STATE TRANSFORMATION MAPS

Any action on a system state ρ can be described by a quantum map. In this Section we present all maps corresponding to realistic, non-ideal measurements in our experiment, to cavity relaxations and to unitary transformations.

Generalized measurement

An unknown quantum state can be estimated by performing measurements on its many identical copies. Each copy can be exposed to a single measurement or to a series of measurements, successively projecting the initial state according to the measurement outcomes. In addition, the system can be subjected, in each realization, to state modifications due to unitary and non-unitary evolutions before and in between the measurements.

The state transformation produced on the state ρ by a specific measurement with outcome μ can be described in terms of a Kraus operator M_μ as

$$\mathbb{M}_\mu(\rho) = \frac{M_\mu \rho M_\mu^\dagger}{\text{Tr}[M_\mu \rho M_\mu^\dagger]}. \quad (1)$$

The product $M_\mu^\dagger M_\mu$ defines a positive operator-valued measure (POVM) for outcome μ . The sum of all possible POVMs for a given measurement equals to unity: $\sum_\mu M_\mu^\dagger M_\mu = I$ [1].

The transformation due to an unread measurement is given by

$$\mathbb{M}_\emptyset(\rho) = \sum_\mu M_\mu \rho M_\mu^\dagger. \quad (2)$$

Resonant atom measurement

Any measurement on the cavity field in our experiment is realized by a controlled atom-cavity interaction followed by atom detection. The resonant interaction with one of the cavities is described by Rabi oscillations between the atom-cavity states $|g, n\rangle$ and $|e, n-1\rangle$ with n photons in the cavity.

One-atom coupling. For each initial atomic state, $|g\rangle$ and $|e\rangle$, there are two Kraus operators describing the cavity state transformation after the atom-cavity interaction and the atomic detection in $|g\rangle$ or $|e\rangle$:

$$\begin{aligned} W_{g,g}(t) &= \sum \cos(\chi_{n-1}t) |n\rangle \langle n|, \\ W_{g,e}(t) &= -i \sum \sin(\chi_{n-1}t) |n-1\rangle \langle n|, \\ W_{e,g}(t) &= -i \sum \sin(\chi_n t) |n+1\rangle \langle n|, \\ W_{e,e}(t) &= \sum \cos(\chi_n t) |n\rangle \langle n|, \end{aligned} \quad (3)$$

where $\chi_n = \Omega_0 \sqrt{n+1}/2$ and Ω_0 is the vacuum Rabi frequency of the atom-cavity interaction. The two indices of W correspond to the initial and detected atomic states, respectively.

Here, we implement two successive resonant interactions of a single atom, initially in $|g\rangle$, with C_1 and C_2 during times t_1 and t_2 , respectively. The Kraus operators $M_g^{[res]}$ and $M_e^{[res]}$, corresponding to an atomic detection in states $|g\rangle$ or $|e\rangle$ after these successive resonant interactions (hence the superscript $[res]$ standing for *resonant*), read

$$\begin{aligned} M_e^{[res]} &= \sum_k W_{g,k}(t_1) \otimes W_{k,e}(t_2), \\ M_g^{[res]} &= \sum_k W_{g,k}(t_1) \otimes W_{k,g}(t_2), \end{aligned} \quad (4)$$

where the sum is taken over two intermediate (ie. between two cavities) atomic states: $k \in \{g, e\}$. The Kraus operators are defined in the product Hilbert space of the two cavities $\{|n_1\rangle \otimes |n_2\rangle\}$. For the resonant probe atom A_2 used in the main paper, we choose $t_1 = \pi/\Omega_0$ and $t_2 = \pi/2\Omega_0$, corresponding to a π -Rabi rotation in C_1 and to a $\pi/2$ -Rabi rotation in C_2 .

Two-atom coupling. The number of atoms n_a per sample obeys a Poisson distribution, $P_a(n_a)$. Atomic samples may thus contain more than one atom. For instance, for a mean atom number equal to 0.1, the probability of having one and two atoms in a sample is $P_a(1) = 9.05\%$ and $P_a(2) = 0.45\%$, respectively (three-atom events can be ignored). Two-atom events have a non-negligible contribution and must be taken into account in the Kraus map construction. In general, two atoms can be prepared and detected in one of the four possible states: $|ee\rangle$, $|eg\rangle$, $|ge\rangle$, and $|gg\rangle$. Their coupling to one cavity during the interaction time t is described by the Kraus operators

$$W_{ee,ee}(t) = \sum \left[1 + \frac{n+1}{2n+3} (\cos(\xi_{n+1}t) - 1) \right] |n\rangle \langle n|, \quad (5)$$

$$W_{ee,eg}(t) = -i \sum \sqrt{\frac{n+1}{2(2n+3)}} \sin(\xi_{n+1}t) |n+1\rangle \langle n|,$$

$$W_{ee,ge}(t) = W_{ee,eg}(t),$$

$$W_{ee,gg}(t) = \sum \frac{\sqrt{(n+1)(n+2)}}{2n+3} (\cos(\xi_{n+1}t) - 1) |n+2\rangle \langle n|,$$

$$W_{eg,ee}(t) = -i \sum \sqrt{\frac{n+1}{2(2n+3)}} \sin(\xi_{n+1}t) |n\rangle \langle n+1|,$$

$$W_{eg,eg}(t) = \frac{1}{2} \sum [1 + \cos(\xi_n t)] |n\rangle \langle n|,$$

$$W_{eg,ge}(t) = \frac{1}{2} \sum [-1 + \cos(\xi_n t)] |n\rangle \langle n|,$$

$$W_{eg,gg}(t) = -i \sum \sqrt{\frac{n+1}{2(2n+1)}} \sin(\xi_n t) |n+1\rangle \langle n|,$$

$$W_{ge,ee}(t) = W_{eg,ee}(t),$$

$$W_{ge,eg}(t) = W_{eg,ge}(t),$$

$$W_{ge,ge}(t) = W_{eg,eg}(t),$$

$$W_{ge,gg}(t) = W_{eg,gg}(t),$$

$$W_{gg,ee}(t) = \sum \frac{\sqrt{(n+1)(n+2)}}{2n+3} (\cos(\xi_{n+1}t) - 1) |n\rangle \langle n+2|,$$

$$W_{gg,eg}(t) = -i \sum \sqrt{\frac{n+1}{2(2n+1)}} \sin(\xi_n t) |n\rangle \langle n+1|,$$

$$W_{gg,ge}(t) = W_{gg,eg}(t),$$

$$W_{gg,gg}(t) = \sum \left[1 + \frac{n}{2n-1} (\cos(\xi_{n-1}t) - 1) \right] |n\rangle \langle n|.$$

Here, all sums start from $n = 0$, $\xi_n = \Omega_0 \sqrt{n+1/2}$ and ξ_{-1} is defined to be zero for the sake of notational convenience. The derivation of these transformations can be found, for instance, in Chapter II.3 of [3].

The successive interaction of two atoms, initially in state $|gg\rangle$, with the two cavities is described by the two-cavity Kraus operators:

$$M_{ee}^{[res]} = \sum_k W_{gg,k}(t_1) \otimes W_{k,ee}(t_2), \quad (6)$$

$$M_{eg}^{[res]} = \sum_k W_{gg,k}(t_1) \otimes W_{k,eg}(t_2),$$

$$M_{eg}^{[res]} = M_{ge}^{[res]},$$

$$M_{gg}^{[res]} = \sum_k W_{gg,k}(t_1) \otimes W_{k,gg}(t_2),$$

where the sum is taken over the four intermediate two-atom states: $k \in \{ee, eg, ge, gg\}$.

Dispersive (QND) atom measurement

We use the dispersive interaction in order to perform a quantum non-demolition (QND) measurement of the joint photon-number parity of the two cavities. It is implemented by the R_1 - R_2 Ramsey interferometer. For an atom-cavity detuning $\delta_{ac}/2\pi \approx 60$ kHz, we achieve a π -phase shift per photon for the atomic $|g\rangle - |e\rangle$ coherence [4, 5]. The interferometer phase is set to maximize the probability for finally detecting the atom in $|g\rangle$ when both cavities are empty. The detection of a dispersive probe atom in $|g\rangle$ or $|e\rangle$ corresponds to the Kraus operators (the superscript $[dis]$ stands for *dispersive*):

$$M_g^{[dis]} = \cos(N\pi/2), \quad (7)$$

$$M_e^{[dis]} = \sin(N\pi/2),$$

where $N = N_1 \otimes I_2 + I_1 \otimes N_2$ is the sum of the photon-number operators N_i of the two cavities (I_i are identity operators).

To a good approximation the simultaneous interactions of two atoms of the same sample with the cavities can be treated separately. The state transformation after detecting two atoms in states s_1 and s_2 is given by the product of the corresponding one-atom operations: $M_{s_1, s_2}^{[dis]} = M_{s_1}^{[dis]} M_{s_2}^{[dis]}$.

Non-ideal atom detection

Any measurement on the cavity field in our experiment is based on atom detection. The number of atoms n_a in each sample follows the Poisson distribution law, $P_a(n_a)$, with the mean atom number of up to 0.2. If we ignore the probability of having more than 2 atoms in a sample, there are six possible detection results:

$\mu' \setminus \mu$	\emptyset	g	e	gg	ee	ge
\emptyset	1	$1-\varepsilon$	$1-\varepsilon$	$(1-\varepsilon)^2$	$(1-\varepsilon)^2$	$(1-\varepsilon)^2$
g	0	$\varepsilon(1-\eta_g)$	$\varepsilon\eta_e$	$2\varepsilon(1-\varepsilon)(1-\eta_g)$	$2\varepsilon(1-\varepsilon)\eta_e$	$\varepsilon(1-\varepsilon)(1-\eta_g+\eta_e)$
e	0	$\varepsilon\eta_g$	$\varepsilon(1-\eta_e)$	$2\varepsilon(1-\varepsilon)\eta_g$	$2\varepsilon(1-\varepsilon)(1-\eta_e)$	$\varepsilon(1-\varepsilon)(1-\eta_e+\eta_g)$
gg	0	0	0	$\varepsilon^2(1-\eta_g)^2$	$\varepsilon^2\eta_e^2$	$\varepsilon^2\eta_e(1-\eta_g)$
ge	0	0	0	$2\varepsilon^2\eta_g(1-\eta_g)$	$2\varepsilon^2\eta_e(1-\eta_e)$	$\varepsilon^2((1-\eta_g)(1-\eta_e)+\eta_g\eta_e)$
ee	0	0	0	$\varepsilon^2\eta_g^2$	$\varepsilon^2(1-\eta_e)^2$	$\varepsilon^2\eta_g(1-\eta_e)$

TABLE S1. Stochastic matrix showing the probability $P(\mu'|\mu)$ to measure outcome μ' for each ideal measurement outcome μ .

$\mu \in \{\emptyset, g, e, gg, ee, ge\}$, where \emptyset denotes no detected atom. The superoperators $\mathbb{L}_\mu^{[\nu]}$ describing the field evolution produced by the interaction $\nu \in \{res, dis\}$ with a sample finally measured in state μ are thus given by

$$\begin{aligned}
\mathbb{L}_\emptyset^{[\nu]} &= P_a(0) \mathbb{I}, \\
\mathbb{L}_g^{[\nu]} &= P_a(1) \mathbb{M}_g^{[\nu]}, \\
\mathbb{L}_e^{[\nu]} &= P_a(1) \mathbb{M}_e^{[\nu]}, \\
\mathbb{L}_{gg}^{[\nu]} &= P_a(2) \mathbb{M}_{gg}^{[\nu]}, \\
\mathbb{L}_{ge}^{[\nu]} &= 2 P_a(2) \mathbb{M}_{ge}^{[\nu]}, \\
\mathbb{L}_{ee}^{[\nu]} &= P_a(2) \mathbb{M}_{ee}^{[\nu]},
\end{aligned} \tag{8}$$

where \mathbb{I} is the unity superoperator.

If the imperfect measurement apparatus is not able to completely distinguish different μ' 's, the real transformation is a mixture of projections of all ideal outcomes μ compatible with the measured result μ' :

$$\mathbb{S}_{\mu'}^{[\nu]}(\rho) = \frac{\sum_\mu P(\mu'|\mu) \mathbb{L}_\mu^{[\nu]}(\rho)}{\text{Tr}[\sum_\mu P(\mu'|\mu) \mathbb{L}_\mu^{[\nu]}(\rho)]}. \tag{9}$$

Here, $P(\mu'|\mu)$ is the probability to obtain μ' for each μ and the sum is taken over all possible measurement results μ [2].

Our non-ideal atom detector has a reduced detection efficiency of $\varepsilon \approx 0.5$, i.e. only one atom out of two is detected on the average. In addition, with the probability of $\eta_g = 0.05$ ($\eta_e = 0.07$), the atomic state $|g\rangle$ ($|e\rangle$) can be erroneously detected as the opposite state $|e\rangle$ ($|g\rangle$). The conditional probabilities $P(\mu'|\mu)$ are given as a stochastic matrix in Table I and explained in detail in [2].

Cavity field relaxation

The cavities have limited lifetimes T_c and a non-zero thermal photon number n_{th} . Therefore, the relaxation of state ρ_i in cavity C_i during a short time interval $\tau = \xi T_c$, with $\xi \ll 1$, can be approximated by the action of the superoperator \mathbb{T} :

$$\mathbb{T}_{i,\tau}(\rho_i) = J_{0,\tau}\rho_i J_{0,\tau}^\dagger + J_{\downarrow,\tau}\rho_i J_{\downarrow,\tau}^\dagger + J_{\uparrow,\tau}\rho_i J_{\uparrow,\tau}^\dagger, \tag{10}$$

where the jump operators are defined as

$$J_{0,\tau} = (1 - \xi n_{th}/2) I - \xi(1/2 + n_{th}) a^\dagger a, \tag{11}$$

$$J_{\downarrow,\tau} = \sqrt{\xi(1 + n_{th})} a, \tag{12}$$

$$J_{\uparrow,\tau} = \sqrt{\xi n_{th}} a^\dagger, \tag{13}$$

with I the identity operator and a the photon-number annihilation operator (we omit the indices i when they are not essential). They describe events in which the photon number changes by 0, -1 and $+1$, respectively (see, eg., [2]). The evolution of the joint two-cavity state is given by the map

$$\mathbb{T}_\tau(\rho) = (\mathbb{T}_{1,\tau} \otimes \mathbb{T}_{2,\tau})(\rho). \tag{14}$$

Unitary transformation maps

Besides the non-unitary measurement- and environment-induced evolutions, the system state ρ undergoes unitary evolutions U corresponding to the generic map

$$\mathbb{U}(\rho) = U\rho U^\dagger. \tag{15}$$

We use coherent amplitude injections in C_i , by means of the microwave source S_i , to provide phase sensitivity to a QND measurement [5] (this is equivalent to a homodyne measurement in quantum optics, giving access to the optical field quadratures). The field injection of a complex amplitude α realizes a unitary displacement $D(\alpha) = \exp(\alpha a^\dagger - \alpha^* a)$, modifying the state ρ_i of cavity C_i as

$$\mathbb{D}_\alpha(\rho_i) = D(\alpha)\rho_i D^\dagger(\alpha). \tag{16}$$

More generally, the simultaneous injection of coherent fields α_1 and α_2 into two cavities is described by the Kraus map

$$\mathbb{D}_{\alpha_1,\alpha_2}(\rho) = (\mathbb{D}_{\alpha_1} \otimes \mathbb{D}_{\alpha_2})(\rho). \tag{17}$$

In the experiment, we detune the frequencies of the two cavities by δ . Their joint state is thus always subject to a unitary evolution, given by the operator

$R(\tau) = \exp(i\delta\tau(N_2 - N_1)/2)$ for an evolution time τ . The corresponding Kraus map reads

$$\mathbb{R}_\tau(\rho) = R(\tau)\rho R^\dagger(\tau). \quad (18)$$

Adjoint maps

The definition (2) of an effect matrix $E^{(r)}$ in the main paper involves adjoint maps, $\{\tilde{\mathbb{K}}_j^{(r)}\}$. The adjoint map $\tilde{\mathbb{K}}$ of \mathbb{K} is defined by

$$\text{Tr}[A\mathbb{K}(B)] = \text{Tr}[\tilde{\mathbb{K}}(A)B] \quad (19)$$

for any Hermitian operators A and B [7]. Therefore, for a map in the general form $\mathbb{K}(\rho) = \sum_i K_i \rho K_i^\dagger$, its adjoint reads

$$\tilde{\mathbb{K}}(\rho) = \sum_i K_i^\dagger \rho K_i. \quad (20)$$

This gives us a simple way for calculating all adjoint maps used in our maximum likelihood reconstruction ($\tilde{\mathbb{S}}^{[res]}$, $\tilde{\mathbb{S}}^{[dis]}$, $\tilde{\mathbb{T}}$, $\tilde{\mathbb{D}}$ and $\tilde{\mathbb{R}}$) via the definition of the corresponding standard maps.

Effect matrices for three experimental sequences

In the main paper we present three types of experimental sequences measuring the two-cavity entangled state. The simplest sequence used for the data shown in Fig. 2(a) consists of a fixed waiting time t (typically, about 1 ms) and a single-resonant-atom interaction. Since decoherence (field relaxation) \mathbb{T} and phase shift \mathbb{R} do not commute, we compute their action over the waiting time t by concatenating small time intervals $\tau = 0.1$ ms, much smaller than $T_{c,1}$ and $T_{c,2}$, in the Trotter approximation spirit. In each time interval, we approximate the evolution by sequential actions of decoherence and phase shift. As a result, the complete effect matrix reads

$$E_{1res}^{(r)} = \left(\tilde{\mathbb{T}}_\tau \circ \tilde{\mathbb{R}}_\tau\right)^{t/\tau} \circ \tilde{\mathbb{S}}_{\mu'}^{[res]}(I/\mathcal{N}_H), \quad (21)$$

where \mathcal{N}_H is the Hilbert space dimension and μ' is the atom detection outcome in realization r .

The measurement sequence used for Fig. 2(b) consists of a field displacement after time t , followed by a sequence of N_s dispersive (QND) atomic samples, separated by time t_a . The corresponding effect matrix reads

$$E_{qnd}^{(r)} = \left(\tilde{\mathbb{T}}_\tau \circ \tilde{\mathbb{R}}_\tau\right)^{t/\tau} \tilde{\mathbb{D}}_{\alpha_1, \alpha_2} \circ \prod_{j=1}^{N_s-1} \left(\tilde{\mathbb{S}}_{\mu'(j)}^{[dis]} \circ \tilde{\mathbb{T}}_{t_a} \circ \tilde{\mathbb{R}}_{t_a}\right) \circ \tilde{\mathbb{S}}_{\mu'(N_s)}^{[dis]}(I/\mathcal{N}_H), \quad (22)$$

with $\mu'(j)$ being the detection result of the sample number j in the realization r .

Finally, the last experimental sequence used for Fig. 2(d) involves N_s resonant atomic samples, separated by t_a , send at time t after the state preparation:

$$E_{Nres}^{(r)} = \left(\tilde{\mathbb{T}}_\tau \circ \tilde{\mathbb{R}}_\tau\right)^{t/\tau} \circ \prod_{j=1}^{N_s-1} \left(\tilde{\mathbb{S}}_{\mu'(j)}^{[res]} \circ \tilde{\mathbb{T}}_{t_a} \circ \tilde{\mathbb{R}}_{t_a}\right) \circ \tilde{\mathbb{S}}_{\mu'(N_s)}^{[res]}(I/\mathcal{N}_H). \quad (23)$$

II. ALGORITHM FOR THE MAXIMUM LIKELIHOOD OPTIMISATION

The maximization of the likelihood function $\mathcal{P}(\varrho)$ is typically realized via the maximization of the concave log-likelihood function

$$f(\rho) = \log \mathcal{P}(\varrho) = \sum_{r=1}^R \log \left(\text{Tr}[\rho E^{(r)}] \right) \quad (24)$$

over the convex closed set of density operators ρ (R is the total number of measurement sequences). This maximization is based on the iterative gradient algorithm with orthogonal projection starting from the initial guess ρ_1 . After the step number k , the state estimate ρ_{k+1} is calculated by

$$\rho_{k+1} = \Pi(\rho_k + g_k \nabla f_k) \quad (25)$$

with

$$\nabla f_k = \sum_{r=1}^R \frac{E^{(r)}}{\text{Tr}[\rho_k E^{(r)}]}, \quad (26)$$

where Π stands for the orthogonal projection onto the set of density operators. It is defined as follows. For any Hermitian operator $X = U\Delta U^\dagger$ with U unitary and Δ diagonal ($\Delta = \text{diag}(\lambda)$), $\Pi(X) = U\Pi(\Delta)U^\dagger$ with $\Pi(\Delta)$ also diagonal and corresponding to the orthogonal projection of the vector $(\lambda_1, \lambda_2, \dots)$ onto the simplex $\{(p_1, p_2, \dots) \mid \forall j, p_j \geq 0, \sum_j p_j = 1\}$. The positive parameter g_k in (25) is chosen such that $g_k \|\nabla^2 f_k\|$ is not too large. We set

$$g_k = -\frac{\text{Tr}[(\nabla f_k)^2]}{\nabla^2 f_k(\nabla f_k, \nabla f_k)}, \quad (27)$$

where Hessian is given by

$$\nabla^2 f_k(X, X) = -\sum \frac{\text{Tr}^2[E^{(r)}X]}{\text{Tr}^2[\rho_k E^{(r)}]}. \quad (28)$$

Our typical initial guess is $\rho_1 = I/\mathcal{N}_H$. Iterations are stopped at step k when the optimality conditions, given

by Eq. (8) in [7], are satisfied up to a numerical tolerance $\epsilon = 10^{-7}$: ρ_{ML} is set to ρ_k when

$$\|\rho_k \nabla f_k - \nabla f_k \rho_k\| \leq \epsilon \|\nabla f_k\|, \quad (29)$$

$$\|P_k \nabla f_k - \lambda_k P_k\| \leq \epsilon \|P_k \nabla f_k P_k\| + \epsilon \|\rho_k\|, \quad (30)$$

$$\lambda_{\min}[\lambda_k I - \nabla f_k] \leq \epsilon \|\lambda_k I\| + \epsilon \|\nabla f_k\|, \quad (31)$$

where $\|X\| = \sqrt{\text{Tr}[X^2]}$ stands for the Frobenius norm of the Hermitian operator X , $\lambda_{\min}(X)$ for its smallest eigenvalue, P_k for the orthogonal projection on the range of ρ_k and $\lambda_k = \text{Tr}[P_k \nabla f_k] / \text{Tr}[P_k]$ (the eigenvalues of ρ_k less than ϵ are set to zero).

III. PRECISION OF THE QUANTUM STATE RECONSTRUCTION

For any Hermitian operator A , the ML estimate of its average value, $\langle A \rangle = \text{Tr}[A \rho_{\text{ML}}]$, admits a standard deviation $\sigma(\langle A \rangle)$ that can be approximated by

$$\sigma^2(\langle A \rangle) \approx \text{Tr}[A_{\parallel} \mathcal{R}^{-1}(A_{\parallel})], \quad (32)$$

where

$$A_{\parallel} = A - \frac{\text{Tr}[A P_{\text{ML}}]}{\text{Tr}[P_{\text{ML}}]} P_{\text{ML}} - (I - P_{\text{ML}}) A (I - P_{\text{ML}}) \quad (33)$$

with P_{ML} the orthogonal projector on the range of ρ_{ML} , see [6] and Eqs. (10)–(11) in [7]. The linear super-operator \mathcal{R} is given by Eq. (11) in [7]. It is self-adjoint and non-negative for the Frobenius scalar product between Hermitian operators. When \mathcal{R} is not positive definite, \mathcal{R}^{-1} corresponds to its Moore-Penrose pseudo-inverse. Numerically, $\mathcal{R}^{-1}(A)$ is obtained via usual linear algebra routines just by considering A as a complex vector of length \mathcal{N}_{H}^2 (where \mathcal{N}_{H} is the dimension of the underlying Hilbert space) and \mathcal{R} as a $\mathcal{N}_{\text{H}}^2 \times \mathcal{N}_{\text{H}}^2$ Hermitian matrix.

Here, we use $\sigma^2(\langle A \rangle)$ to calculate the error bars of the reconstructed density matrix ρ_{ML} . The density matrix element ρ_{pq} is, in general, complex and we use the following standard notations:

$$\begin{aligned} x_{pq} &= \text{re}(\rho_{pq}), \\ y_{pq} &= \text{im}(\rho_{pq}), \\ \phi_{pq} &= \text{arg}(\rho_{pq}), \\ r_{pq} &= \text{abs}(\rho_{pq}) = |\rho_{pq}|. \end{aligned} \quad (34)$$

We denote $\sigma(x_{pq})$ and $\sigma(y_{pq})$ the precision (ie. error bars) of the real (x_{pq}) and imaginary (y_{pq}) parts of a reconstructed density matrix element ρ_{pq} , respectively. These precisions are equal to $\sigma(x_{pq}) = \sigma(\langle X^{(pq)} \rangle)$ and $\sigma(y_{pq}) = \sigma(\langle Y^{(pq)} \rangle)$, calculated for the following operators:

$$\begin{aligned} X^{(pq)} &= \frac{|p\rangle \langle q| + |q\rangle \langle p|}{2}, \\ Y^{(pq)} &= i \frac{|p\rangle \langle q| - |q\rangle \langle p|}{2}. \end{aligned} \quad (35)$$

Knowing the simple dependence of ϕ_{pq} and r_{pq} on x_{pq} and y_{pq} , we easily get the corresponding precision of the phase and the absolute value of ρ_{pq} :

$$\begin{aligned} \sigma(\phi_{pq}) &= \frac{\sqrt{[y_{pq} \sigma(x_{pq})]^2 + [x_{pq} \sigma(y_{pq})]^2}}{r_{pq}^2}, \\ \sigma(r_{pq}) &= \frac{\sqrt{[x_{pq} \sigma(x_{pq})]^2 + [y_{pq} \sigma(y_{pq})]^2}}{r_{pq}}. \end{aligned} \quad (36)$$

IV. RECONSTRUCTED DENSITY MATRICES

All reconstructions presented in the paper have been realized in the Hilbert space dimension $\mathcal{N}_{\text{H}} = 5 \times 5$. However, for the sake of clarity, in the main text of the paper we plot the reconstructed density matrices limited to 2 photons (see Fig. 2 of the main paper). Here, in Fig. S1, we show full reconstructed density matrices of size $5^2 \times 5^2$. The fidelity of states (a)-(d) with respect to the expected one is 0.29, 0.85, 0.96 and 0.78, respectively. Numerical values of all presented density matrices, as well as their error bars, are given in additional files, compressed in an attached zip archive.

V. BOOTSTRAPPING METHOD FOR RECONSTRUCTION PRECISION ESTIMATION

We implement a bootstrapping approach to estimate the reconstruction precision of the quantum superposition phase ϕ_a as a function of the sample size (number of different realizations R used for the reconstruction). First, we perform 18000 realizations with 40 resonant atomic samples, similar to those used for Fig. 2(d). The set of computed effect matrices $\{E^{(r)}\}$ is randomly split into independent groups of size R ($100 \leq R \leq 9000$). Using each group separately, we reconstruct ρ_{ML} , determine the estimate ϕ of ϕ_a and compute its error bar $\sigma(\phi)$. With all groups of the same size R , we calculate the standard deviation $\tilde{\sigma}_{\phi, R}$ of the reconstructed values of ϕ and the mean value $\langle \sigma(\phi) \rangle_R$ of the computed error bar $\sigma(\phi)$. This procedure is repeated 4 times with different group samplings and the results are finally averaged.

-
- * Current affiliation: Faculty of Physics, University of Vienna, Boltzmanngasse 5, A-1090 Vienna, Austria
- [1] S. Haroche and J.M. Raimond, *Exploring the Quantum: atoms, cavities and photons*, Oxford University Press, Oxford (2006).
- [2] B. Peaudecerf, C. Sayrin, X. Zhou, T. Rybarczyk, S. Gleyzes, I. Dotsenko, J. M. Raimond, M. Brune, and S. Haroche, *Quantum feedback experiments stabilizing Fock states of light in a cavity*, Phys. Rev. A **87**, 042320 (2013).

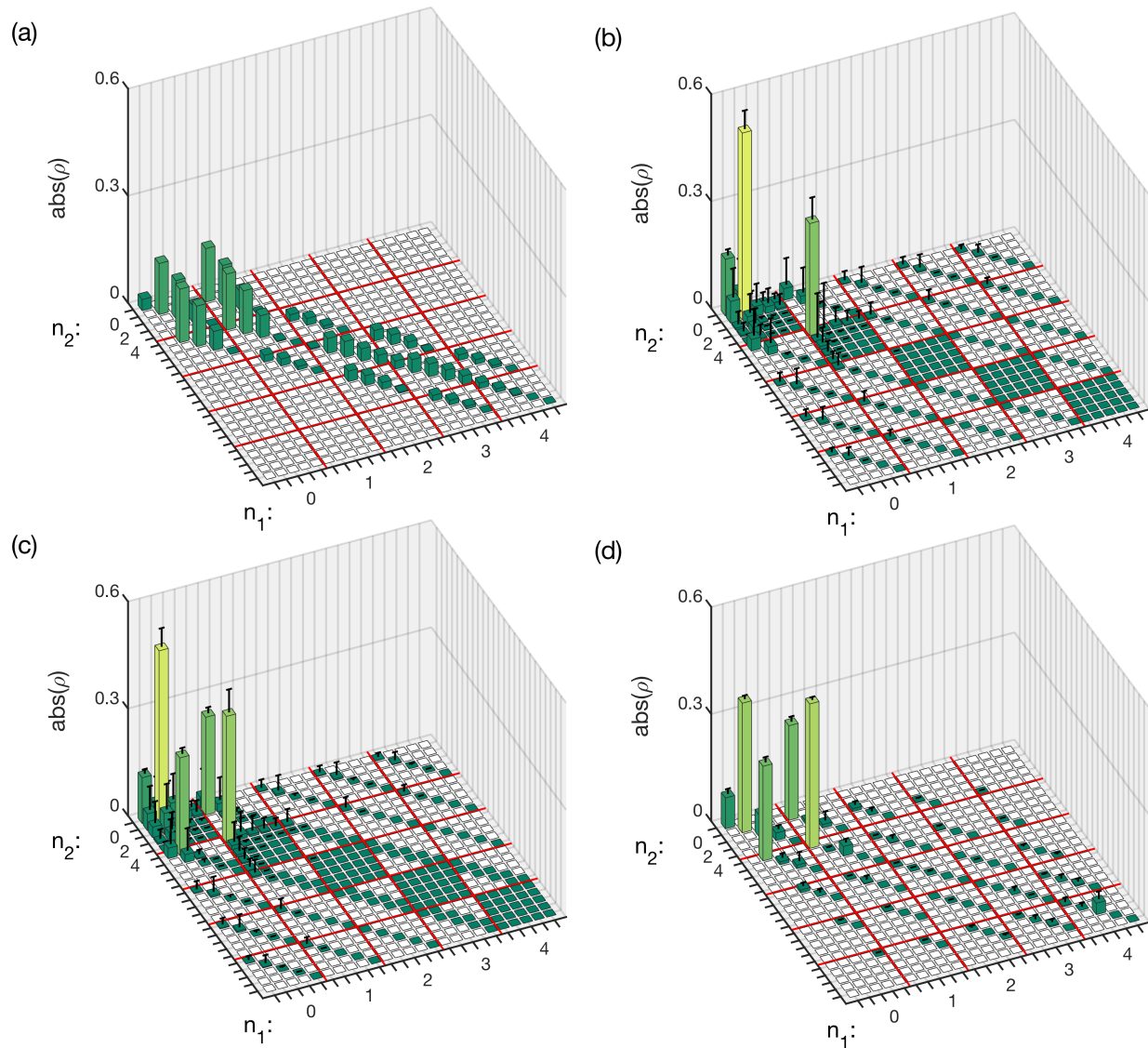


FIG. S1. Density matrix absolute values in a 5×5 two-cavity Hilbert space. Red guiding lines enclose areas with the same photon number in C_1 . Blank elements correspond to zero elements in all $E^{(r)}$, see main text for details.

- (a) Reconstruction based on single resonant-atom measurements.
 (b) Reconstruction based on QND parity measurement.
 (c) Reconstruction with both resonant and dispersive data of (a) and (b).
 (d) Reconstruction with sequences of several resonant atoms.

Error bars $\sigma(\text{abs}(\rho_{\text{ML}}))$ in (a) are of the order of 0.5 and are not shown. Error bars smaller than 10^{-3} are not shown in plots (b)-(d).

[3] Xingxing Zhou, *Field locked to Fock state by quantum feedback with single photon corrections*, PhD thesis, Universit  Pierre et Marie Curie - Paris VI (2012), <https://tel.archives-ouvertes.fr/tel-00737657>
 [4] S. Gleyzes, S. Kuhr, C. Guerlin, J. Bernu, S. Del glise, U. Busk Hoff, M. Brune, J.-M. Raimond, and S. Haroche, *Quantum jumps of light recording the birth and death of a photon in a cavity*, Nature (London) **446**, 297 (2007).
 [5] S. Del glise, I. Dotsenko, C. Sayrin, J. Bernu, M. Brune, J.M. Raimond, and S. Haroche, *Reconstruction of non-*

classical cavity field states with snapshots of their decoherence, Nature (London) **455**, 510 (2008).
 [6] P. Six and P. Rouchon, *Feedback Stabilization of Controlled Dynamical Systems*, chapter *Asymptotic expansions of Laplace integrals for quantum state tomography*, Lecture Notes in Control and Information Sciences 473, pp. 307–327, Springer (2017).
 [7] P. Six, Ph. Campagne-Ibarcq, I. Dotsenko, A. Sarlette, B. Huard, and P. Rouchon, *Quantum state tomography with noninstantaneous measurements, imperfections, and decoherence*, Phys. Rev. A **93**, 012109 (2016).